Research in Astronomy and Astrophysics, 23:015014 (8pp), 2023 January https://doi.org/10.1088/1674-4527/aca234

Mass Distribution of Black Holes with Effects of Convective Carbon Shell Burning on Pair-instability Pulsation and Fe Core Collapse

Wenyu Xin[1,2], Ken'ichi Nomoto[3], Gang Zhao[1,2], and Xianfei Zhang[4]
[1] CAS Key Laboratory of Optical Astronomy, National Astronomical Observatories, Chinese Academy of Sciences, Beijing 100101, China; gzhao@nao.cas.cn
[2] School of Astronomy and Space Science, University of Chinese Academy of Sciences, Beijing 100049, China
[3] Kavli Institute for the Physics and Mathematics of the Universe (WPI), The University of Tokyo Institutes for Advanced Study, The University of Tokyo, Kashiwa, Chiba 277-8583, Japan; nomoto@astron.s.u-tokyo.ac.jp
[4] Department of Astronomy, Beijing Normal University, Beijing 100875, China
Received 2022 October 9; revised 2022 October 28; accepted 2022 November 2; published 2022 December 21

Abstract

Motivated by the determination of black hole masses with gravitational-wave observations, we calculate the evolution of massive stars through presupernova stages and obtain the mass distribution of black holes. In the first part, we calculate the evolution of He stars with masses of 30–120 $M_{\odot}$. We study in detail how convective carbon shell burning controls pair-instability pulsations before and during oxygen burning and determine their final fates. In the second part, we calculate the evolution of H-rich stars with initial masses of 13–80 $M_{\odot}$ until Fe core collapse and obtain the possible black hole mass range by applying the criterion of the compactness parameters. From these models, we predict the mass distribution of black holes for stars that undergo Fe core collapse and pair-instability pulsation. The predicted masses for black holes range from 4.2 to 46 $M_{\odot}$, which are consistent with the gravitational-wave observations.

Key words: gravitational waves – stars: black holes – stars: evolution – stars: massive – (stars:) supernovae: general

1. Introduction

Detections of gravitational waves (GWs) have provided a new probe to explore the mass distribution of stellar-mass black holes (BHs) (Abbott et al. 2016, 2019). By now, most of the merging binary BHs (BBHs) confirmed by GWs with LIGO/VIRGO are several tens of solar masses, which fall in the mass range allowed by the stellar evolution theory except for the GW190521 (85^{+21}_{-14} $M_{\odot}$ and 66^{+17}_{-18} $M_{\odot}$; Abbott et al. 2020). The probability that at least one of them falls in the predicted pair-instability supernovae (PISNe) mass gap (50–140 $M_{\odot}$) is 99.0%, which is a significant challenge to the theory of stellar evolution and PISNe (Fowler & Hoyle 1964; Barkat et al. 1967; Woosley 2017).[5]

In close binary systems, stars with zero-age main-sequence (ZAMS) mass of $M(\mathrm{ZAMS}) > 80\ M_{\odot}$ form He stars with initial mass of $M(\mathrm{He}) > 35\ M_{\odot}$ at the end of He burning and undergo electron–positron pair instability after carbon burning. The oxygen core collapses, and oxygen burning becomes explosive. Then, three further evolutions and fates are distinguished according to M(ZAMS) (e.g., see Nomoto et al. 2013 for a review). (1) For stars with $M(\mathrm{ZAMS}) = 80$–$140\ M_{\odot}$ (which form He stars of $M(\mathrm{He}) = 35$–$65\ M_{\odot}$), explosive oxygen burning causes several pulsations (pulsational pair instabilities; PPIs; Barkat et al. 1967). Some pulsations are strong enough to induce mass ejection. Eventually, these He stars evolve to form Fe cores and collapse into compact objects (PPI supernova; PPISN), whose masses are smaller than the initial masses of He stars. (2) For stars with $M(\mathrm{ZAMS}) \sim 140$–$300\ M_{\odot}$ (which form He stars with initial masses of $M(\mathrm{He}) \sim 65$–$140\ M_{\odot}$), the energy released from explosive oxygen burning is large enough to disrupt the whole star (Barkat et al. 1967; Baraffe et al. 2001; Umeda & Nomoto 2002b), which is called a PISN. (3) Stars with $M(\mathrm{ZAMS}) > 300\ M_{\odot}$ ($M(\mathrm{He}) > 140\ M_{\odot}$) collapse into BHs as a consequence of the photodisintegration instability.

The physical mechanism of PPISN/PISN is well understood (Fowler & Hoyle 1964; Barkat et al. 1967; Bond et al. 1984; Heger & Woosley 2002; Umeda & Nomoto 2002a; Chen et al. 2014; Marchant et al. 2019; Leung et al. 2020). However, there are still uncertainties in the maximum mass of BHs $M(\mathrm{BH})_{\mathrm{max}}$. Farmer et al. (2019) investigated the sensitivity on many factors, including mass loss, metallicity, nuclear reaction network, reaction rates and numerical resolution. In addition, the effects of convection (Renzo et al. 2017), rotation (Marchant et al. 2019; Woosley & Heger 2021) and super-Eddington accretion (van Son et al. 2020) are also reported. Among these uncertainties, the effect of $^{12}\mathrm{C}\ (\alpha, \gamma)^{16}\mathrm{O}$ reaction rate seems to be the most important (e.g., Farmer et al. 2020; Costa et al. 2021; Woosley & Heger 2021). In these three works, the impact mechanism of $^{12}\mathrm{C}\ (\alpha, \gamma)^{16}\mathrm{O}$ reaction is attributed to convective carbon shell burning, but none of them

[5] In the following discussion, we assume that stars have low-enough metallicities for a wind-type mass loss to be negligible (e.g., see Limongi & Chieffi 2015 for the wind effect on the core mass).

discussed how it prevents the contraction of the oxygen core in detail.

In the first part of the present work, we calculate the evolution of He stars that undergo PPISN/PISN and obtain the BH mass spectrum of the PPISN models. In particular, we focus on the interpretation of how convective carbon shell burning affects the BH mass spectrum. On the other hand, massive stars with $M(\mathrm{ZAMS}) < 80\ M_{\odot}$ (corresponding to $M(\mathrm{He}) < 35\ M_{\odot}$) undergo core-collapse supernova (CCSN). After Fe cores are formed, some progenitors (usually $M(\mathrm{ZAMS}) < 25\ M_{\odot}$) explode and leave neutron stars as remnants, while others collapse into BHs.

In the second part of this work, we study the evolution of stars with $M(\mathrm{ZAMS}) = 13$–$80\ M_{\odot}$ through pre-CCSN to obtain the BH mass spectrum. Then, we compare the BH mass spectrum with that of the BBHs reported by LIGO/VIRGO.

This paper is organized as follows. In Section 2, we describe the He star models and input physics. In Section 3, the stars in close binary systems are discussed briefly. The evolution of He stars and convective carbon shell burning are discussed in Section 4. Finally, we present the compactness parameters of presupernova models and discuss the mass distribution of BH produced by both CCSN and PPISN in Sections 5 and 6, respectively.

2. Models and Input Physics

2.1. He Star Models

For He stars with initial masses $M(\mathrm{He}) = 30$–$120\ M_{\odot}$, we calculated the evolution from zero-age horizontal branch (ZAHB) through the following stages: (1) Fe core collapse (CC) without PPI, (2) the PPI and then Fe CC (PPISN) and (3) PISNe.

For initial elemental abundances, we assumed the He mass fraction of $Y = 0.999$ and the metallicity of $Z = 10^{-3}$, which denotes the sum of the initial mass fraction of elements heavier than ^{4}He. The initial abundances of heavier elements follow Anders & Grevesse (1989).

For the hydrostatic evolution of He stars (before PPIs), we used the Modules for Experiments in Stellar Astrophysics (MESA, version 12778; Paxton et al. 2011, 2013, 2015, 2018, 2019).

During the PPI, explosive oxygen burning decreases the nuclear timescale to a comparable level of the dynamic timescale so that the hydrostatic approximation may no longer work well. Then, the hydrodynamic module is required to follow the evolution during the PPI (Woosley 2017; Leung et al. 2019). We adopted the one-dimensional implicit hydrodynamics option. Instead of the artificial viscosity introduced by Paxton et al. (2015), another option using the approximate Riemann solver was adopted in this work. The Harten–Lax–van Leer–contact (HLLC) solver method (Toro et al. 1994) provides improved shock capturing and energy conservation. The detailed implementation of this scheme is documented by Paxton et al. (2018). We used the HLLC solver only for the hydrodynamic phase.

To avoid the PPI being interrupted by the code stop control, we set a very large value for the limit of inward velocity of the Fe core (`fe_core_infall_limit=1d99`). The CC (Fe CC without PPI) would cease when the central temperature exceeds 10^{10} K. For other parameters, which may also affect the evolution of massive stars, we used the default and recommended values in the package, namely "ppisn."

2.2. H-rich Star Models

For the hydrostatic evolution from ZAMS of H-rich stars with $M(\mathrm{ZAMS}) = 13$–$80\ M_{\odot}$, we used the same MESA code as used for He stars. We adopted metallicities of $Z = 0.02$ and $Z = 10^{-5}$ whose initial abundances of heavier elements also follow Anders & Grevesse (1989).

2.3. Input Physics

In the convection zone, we used the mixing-length theory with the ratio between the mixing length and the pressure scale height of $\alpha_{\mathrm{mlt}} = 2.0$. Overshooting was treated with exponential type, with $f_0 = 0.005$ and $f_{\mathrm{ov}} = 0.01$.

The Dutch scheme was adopted for mass loss with `Dutch_scaling_factor=0.5`. Three main mass-loss prescriptions experienced in the Dutch scheme are from de Jager et al. (1988) for cool stars, Vink et al. (2001) for hot H-rich stars, and Nugis & Lamers (2000) for Wolf–Rayet stars.

Previously, Farmer et al. (2019) found that the size of the network had little effect on the final BH masses, and hence, the present work will not study the details of nucleosynthesis. Here, `basic.net`, `co_burn.net` and `approx21.net` were adopted for H and He burning, carbon and oxygen burning, and later evolution, respectively. These networks cover the α-chain reactions up to ^{28}Si, main reactions in the carbon and oxygen burning stages, and reactions with 21 isotopes for the final evolution, respectively. The reaction rates of $^{12}\mathrm{C}\ (\alpha, \gamma)^{16}\mathrm{O}$ from Kunz et al. (2002) and $^{12}\mathrm{C}+^{12}\mathrm{C}$ from Tumino et al. (2018) were adopted. Other reaction rates were taken from ReaclibV2.2 (Cyburt et al. 2010). For weak interactions, the tabulations of Langanke & Martínez-Pinedo (2000), Oda et al. (1994) and Fuller et al. (1985) were adopted.

3. Massive Stars in Close Binary System

The majority of massive stars are born in binary systems (Kobulnicky et al. 2014), and more than 70% of them exchange materials with their companion stars (Moe & Di Stefano 2017). Due to the enhanced mass loss from stellar winds and the interaction with the binary companions, the massive stars in close binary systems tend more likely to form He stars. In this section, we discuss the formation and evolution of He stars.

3.1. Wind-type Mass Loss

For the effect of the wind-type mass loss, Leung et al. (2019) discussed the parameter dependences of the He core mass formed after H exhaustion at the center for $M(\mathrm{ZAMS}) = 80$–$160\,M_\odot$. According to their results, the metallicity adopted for our He stars is consistent with the formation of He cores of $M(\mathrm{He}) = 30$–$120\ M_\odot$, which includes the He core mass range for PPISNe/PISNe.

For H-rich stars, the effect of wind-type mass loss is weak, so that the star retains a significant fraction of its H-rich envelope at H exhaustion.

3.2. Roche-lobe Overflow

In close binary systems, we assume the companion is a neutron star or a BH. Once the radii of stars increase to overfill their Roche lobes, mass transfer starts. The evolutionary stage when the mass transfer starts depends on the initial orbital separation of binaries. In some close binary systems, the mass transfer may occur when the donor stars still undergo core H burning, which is called case A mass transfer. Case B transfer occurs just after core H burning. Case C mass transfer occurs when the donor star climbs the giant branch. This case exists for wide separation binary systems. We assume that binaries are close enough for case A and case B mass transfer to occur, which may remove all the H-rich envelope of stars (Wellstein et al. 2001). Since discussion about the complex mass transfer phase was not the aim of this work, we focus on the evolution of He stars formed after the Roche-lobe overflow.

4. Evolution of He Stars

In this section, we describe the first part of our calculations, i.e., the evolution of He stars.

4.1. Evolution from ZAHB

We calculated the evolution of He stars from ZAHB. They undergo CC for $M(\mathrm{He}) \leqslant 40\ M_\odot$, PPISNe for $44 \leqslant M(\mathrm{He}) \leqslant 76\ M_\odot$ and PISNe for $M(\mathrm{He}) \geqslant 76\ M_\odot$. If we assume the mass of BH as the He star mass at the CC and PPISN, i.e., no mass ejection during the collapse, the maximum BH mass would be $\sim$46 $M_\odot$. This result is in agreement with that reported by Farmer et al. (2019, 2020) (45 $M_\odot$ for $Z = 0.001$ case) and Leung et al. (2019). Woosley & Heger (2021) also showed $M(\mathrm{BH})_{\max} = 46\ M_\odot$ for the $^{12}\mathrm{C}\ (\alpha,\ \gamma)^{16}\mathrm{O}$ reaction rate enhanced by a factor of 1.2. This reaction rate used in Woosley & Heger (2021) comes from Buchmann et al. (1996), which is considered to be a better value after this enhancement (Tur et al. 2007; Woosley & Heger 2007).

Main information and the final fate of our He star models are shown in Table 1. $X(^{12}\mathrm{C})$ and $M(\mathrm{CO})$ are the mass fraction of $^{12}\mathrm{C}$ and the CO core mass at the end of He burning when $X(^4\mathrm{He})$ becomes lower than 10^{-4} at the center. We define $M(\mathrm{CO})$ as an enclosed mass, M_r, at the shell, where X changes inwardly from $X \geqslant 10^{-4}$ to $X < 10^{-4}$. $\Delta M(\mathrm{wind})$ and $\Delta M(\mathrm{ppi})$ show mass loss due to stellar winds and PPIs. As an example, the central temperature against the central density for $M(\mathrm{He}) = 36\,M_\odot$ (green; CC) and $64\,M_\odot$ (red; PPISN) are compared in Figure 1. Different from the model of $M(\mathrm{He}) = 36\ M_\odot$, which directly undergoes CC, two pulses occur during oxygen burning for $M(\mathrm{He}) = 64\ M_\odot$. The first pulse is strong enough to eject 4.88 $M_\odot$, while the second pulse is too weak to give rise to mass loss.

Table 1
Information of $M(\mathrm{He})$, $M(\mathrm{CO})$, Mass Loss, Mass Fraction of $^{12}\mathrm{C}$ and the Final Fate for the He Star Models

$M(\mathrm{He})$	$M(\mathrm{CO})$	$\Delta M(\mathrm{wind})$	$\Delta M(\mathrm{ppi})$	$M(\mathrm{final})$	$X(^{12}\mathrm{C})$	Fate
30	21.90	3.84	0	26.14	0.187	CC
32	23.61	4.31	0	27.69	0.181	CC
36	26.39	5.28	0	30.72	0.169	CC
40	29.16	6.31	0	33.69	0.159	CC
44	23.88	7.40	0.03	36.56	0.151	PPISN
48	26.50	8.55	0.97	38.48	0.143	PPISN
52	28.10	9.74	0.05	42.21	0.137	PPISN
56	29.88	11.01	1.47	43.54	0.131	PPISN
60	38.23	12.29	1.89	45.82	0.125	PPISN
64	40.99	13.61	4.88	45.51	0.120	PPISN
68	38.23	14.97	9.68	43.35	0.116	PPISN
72	36.71	16.36	15.15	40.49	0.112	PPISN
76	33.17	17.72	22.82	35.46	0.108	PPISN
80	51.35	19.14	60.86	0	0.104	PISN
84	53.66	20.06	63.94	0	0.101	PISN
86	54.77	21.30	64.70	0	0.099	PISN
88	55.90	22.10	65.90	0	0.098	PISN
96	60.20	25.26	70.74	0	0.092	PISN
98	61.25	26.07	71.93	0	0.091	PISN
104	68.00	28.52	75.48	0	0.088	PISN
112	72.36	31.92	80.08	0	0.084	PISN
120	76.52	35.41	84.59	0	0.080	PISN

4.2. Shell Carbon Burning

During core He burning, most $^{12}\mathrm{C}$ produced by the 3α reaction is converted to $^{16}\mathrm{O}$ by the $^{12}\mathrm{C}\ (\alpha,\ \gamma)^{16}\mathrm{O}$ reaction. Figure 2 shows that the mass fraction of $^{12}\mathrm{C}$, $X(^{12}\mathrm{C})$, decreases for larger $M(\mathrm{He})$ at the end of core He burning. This result agrees well with that of Woosley & Heger (2021) and Costa et al. (2021).

After core He burning, the CO core contracts. As the temperature increases, once the nuclear energy generation rate ϵ_{C} exceeds the energy loss rate by neutrino emissions ϵ_ν, carbon burns convectively to carry out the excess energy. According to the definition of ϵ_{C} and ϵ_ν as well as $m^2 \sim T^3\rho^{-1}$ for ideal gas, the maximum of ϵ_{C} and ϵ_ν is scaled as

$$\frac{\epsilon_{\mathrm{C}}}{\epsilon_\nu}\Big|_{\max} \sim X(\mathrm{C})^{1.4}\frac{\mathrm{d}T}{\mathrm{d}t}^{0.6} m^{-2.8} \quad (1)$$

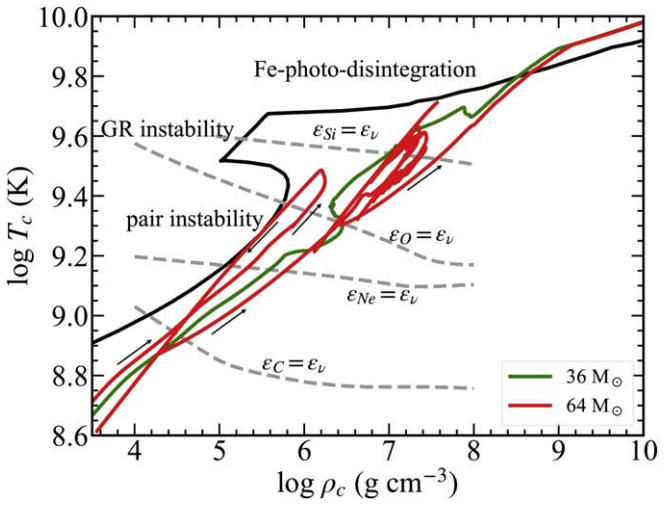

Figure 1. The central temperature against the central density for $M(\mathrm{He}) = 36$ and 64 $M_\odot$. The region on the left of the black line represents regimes dominated by the dynamic instability due to the pair creation, general relativistic (GR) effects (e.g., see Osaki 1966) and the photodisintegration of matter in nuclear statistical equilibrium at $Y_e = 0.5$ (Ohkubo et al. 2009).

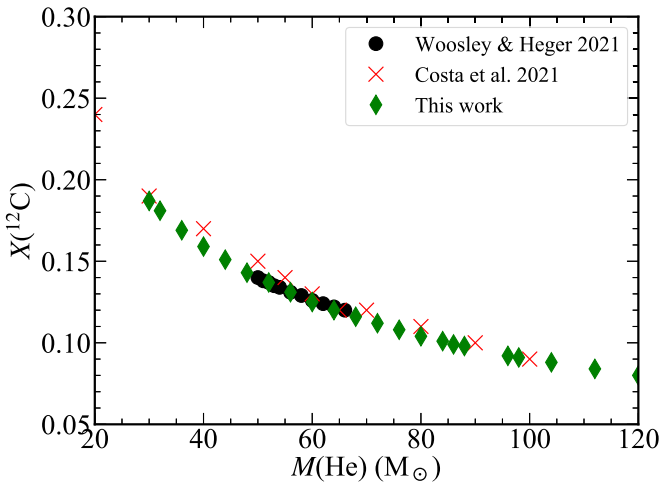

Figure 2. The mass fraction of ^{12}C, $X(^{12}\mathrm{C})$, at the center as a function of the initial mass of He, M(He). The green diamonds indicate our results. The red crosses and black points are those from Costa et al. (2021) and Woosley & Heger (2021), respectively.

in Sukhbold & Adams (2020), where m denotes the stellar mass. Because the temperature changes little during carbon burning, with larger M(He) and smaller $X(^{12}\mathrm{C})$, the maximum of the ratio ϵ_C and ϵ_ν decreases. There exists the following critical mass M_crit. When $M > M_\mathrm{crit}$, $\epsilon_\mathrm{C} \geqslant \epsilon_\nu$ is not satisfied, and carbon should burn radiatively.

In the top row of Figure 3, we show the Kippenhahn diagrams from carbon burning up to the ignition of oxygen burning for different M(He). For lower mass ($M(\mathrm{He}) = 36\ M_\odot$), $X(^{12}\mathrm{C}) \sim 0.17$ in the CO core after core He burning. Carbon is ignited at the off-center shell ($M_r = 2.0\ M_\odot$) after 1800 yr of He exhaustion. With carbon consumption, the carbon burning shell moves outward up to $M_r = 10.0\ M_\odot$. After the convection occurs (marked by purple diamonds) and extends to the outer boundary of the CO core, the bottom of the carbon burning shell stops moving outward and keeps burning at $M_r = 4.0\ M_\odot$. Because the convection transfers the fresh fuel from the outer layer of the CO core, $X(^{12}\mathrm{C})$ at the bottom of the carbon burning shell changes, as shown in the middle row of Figure 3. With enough fuel, carbon shell burns actively and releases enough energy to prevent the dynamic contraction of the core. The result of this heating effect is shown in the bottom row of Figure 3. The temperature increases slowly and keeps constant after the oxygen ignition at the center. Thus, oxygen burning is stable without giving rise to PPI.

For the intermediate mass ($M(\mathrm{He}) = 64\ M_\odot$), the carbon burning shell is less energetic because of the smaller $X(^{12}\mathrm{C})$ ($\sim$0.12). And ϵ_C is proportional to the square of $X(^{12}\mathrm{C})$. The central temperature increases rapidly because of the unstable contraction of the core. Only $\sim$1 day after the convection appears, T_c exceeds $10^{9.4}$ K, which can ignite explosive oxygen burning. Due to the short time and inactive carbon shell burning, the convective region cannot extend to the outer layer to transfer the fuel. Once explosive oxygen burning is ignited, convection can efficiently transport the released energy to the outer shell. The total energy of the star is still negative. Then, the star is not disrupted and pulsations take place.

For the higher mass ($M(\mathrm{He}) = 86\ M_\odot$), $X(^{12}\mathrm{C}) < 0.1$ in the core. Without an active carbon burning shell, T_c increases more quickly. The time from the ignition of carbon shell burning to the ignition of explosive oxygen burning is less than one month. Although a convective core forms after the oxygen ignition, it is not efficient enough to transport such a large amount of nuclear energy. Then, the total energy of the star becomes positive. As a result, the whole star is disrupted.

Here, the relation between convective carbon shell burning and the final fate of stars is summarized as follows:

1. Before the central oxygen ignition, a convective shell extends to an outer region to mix the carbon fuel to the carbon burning shell and maintain carbon shell burning energetic. Active carbon shell burning heats the surrounding region and retards the contraction of the core. After the oxygen ignition, the convection can efficiently transport the excess energy and ensure steady oxygen burning. Thus, stars undergo CC.

2. Before the central oxygen ignition, a convection shell is not large enough to supplement the carbon fuel to the carbon burning shell. Then, the oxygen core rapidly contracts to ignite explosive oxygen burning. The resultant convective region is large enough to transfer the produced energy and keeps the total energy of the star negative. Then, the star undergoes a PPISN.

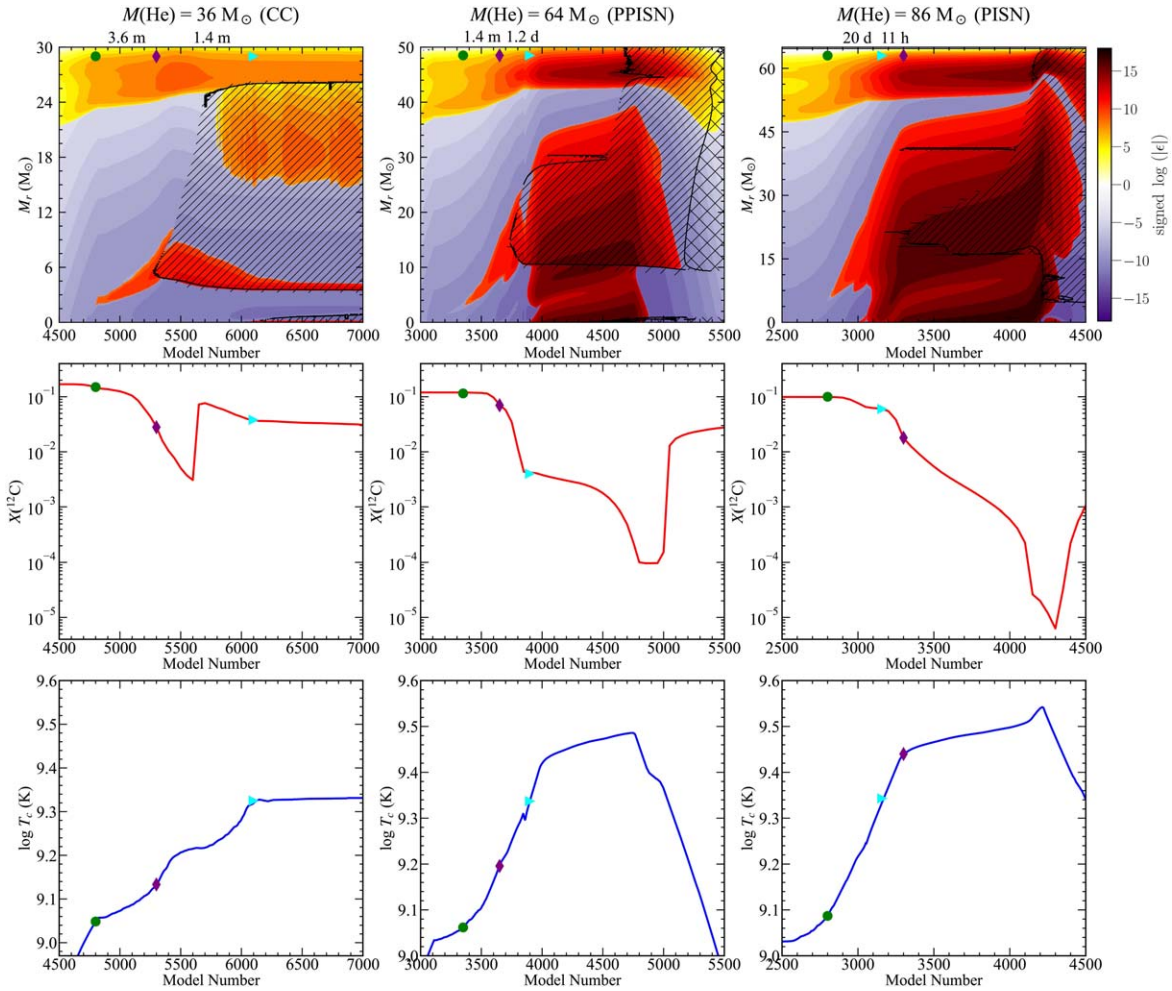

Figure 3. The time evolution of core structure of stars for $M(\mathrm{He}) = 36$, 64 and 86 $M_\odot$, which undergo CC, PPISN and PISN, respectively. The green points, purple diamonds and cyan triangles indicate the location of shell carbon burning ignition, core oxygen burning ignition and convection occurrence. The m, d and h represent the units of month, day and hour. The top row shows the Kippenhahn diagrams from the end of helium burning to the oxygen burning. The colorbar shows the signed logarithm of the energy generation rate, i.e., $\mathrm{sign}(\epsilon_{\mathrm{nuc}} - \epsilon_\nu)\log(|\epsilon_{\mathrm{nuc}} - \epsilon_\nu|)/(\mathrm{erg\ g^{-1}\ s^{-1}})$, where ϵ_{nuc} is the energy generation rate of nuclear reactions and ϵ_ν is the neutrino loss rate. The strong neutrino cooling and strong nuclear burning are denoted by purple and red regions, while the convective regions are indicated by hatched regions. The last two rows show the evolution of $X(^{12}\mathrm{C})$ at the bottom of carbon shell burning and the temperature at the center, respectively.

3. The carbon convective region is too small to mix fuel into the shell and forms too late to prevent the contraction of the oxygen core. Then, oxygen burning is explosive enough to accumulate the energy in the core. The total energy of the star becomes positive, and the whole star explodes as a PISN.

5. Evolution of H-rich Stars and Compactness Parameters for CCSN

In the second part of the present work, we calculated the evolution of H-rich stars of $M(\mathrm{ZAMS}) = 13$–$80\,M_\odot$ from ZAMS to the final stage when the temperature reaches 10^{10} K at the center. We adopted two metallicities of $Z = 0.02$ (solar) and $Z = 10^{-5}$ (metal-poor). The evolution is similar to earlier works (e.g., Sukhbold et al. 2016, 2018 and Chieffi et al. 2021), and the details will be published elsewhere. In the present work, we focus on the final fate of CC, i.e., which star collapses to form a BH and how much is the BH mass for comparison with the GW observations.

For the final fate of CC, O'Connor & Ott (2011) and Ertl et al. (2016) introduced the compactness parameter, $\xi_{2.5}$, and a two-parameter criterion to predict whether presupernova models explode or collapse. The compactness parameter (ξ_M) is defined as:

$$\xi_M = \frac{M/M_\odot}{r(M)/1000\ \mathrm{km}} \tag{2}$$

with $r(M)$ the radius at $M_r = M$. We assume that the star collapses into a BH when the compactness parameter at

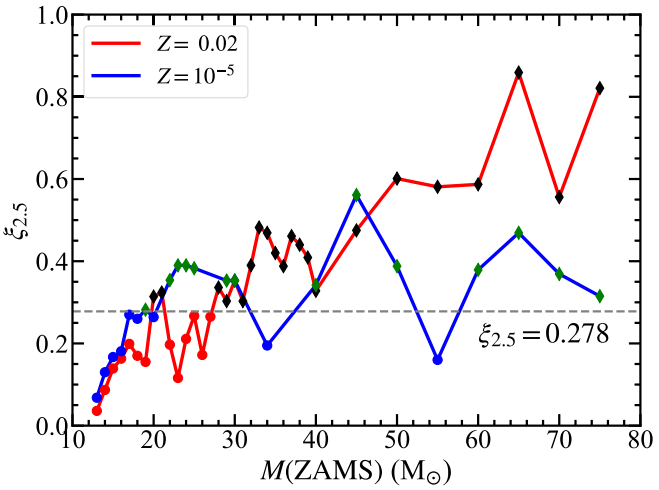

Figure 4. The compactness parameter, $\xi_{2.5}$, as a function of M(ZAMS). All the models are distinguished by the gray line of $\xi_{2.5} = 0.278$. The points are used to show the exploding models, while the diamonds represent the models that collapse into BH.

$M_r = 2.5\,M_\odot$, $\xi_{2.5} > 0.278$ (Müller et al. 2016) at the final stage and that the star explodes to form a neutron star if $\xi_{2.5} < 0.278$.

Figure 4 shows that $\xi_{2.5}$ of both solar-metallicity stars and metal-poor stars change with M(ZAMS) non-monotonically. For stars with the solar metallicity, the compactness parameter shows several peaks. The peak near M(ZAMS) = 21 $M_\odot$ forms because it is near the boundary mass between the convective and radiative central carbon burning, which was discussed by Chieffi et al. (2021) as follows. Without a convective carbon burning core, $\xi_{2.5}$ increases sharply due to the contraction of the CO core. On the other hand, convective carbon shell burning reduces $\xi_{2.5}$ for M(ZAMS) = 21–23 $M_\odot$. A small peak of $\xi_{2.5}$ forms near M(ZAMS) = 25 $M_\odot$. Although only one model may collapse to a BH, such a case is important. (With a mass interval of 0.1 $M_\odot$, Chieffi et al. (2021) found a similar peak at M(ZAMS) = 24.2–26 $M_\odot$.)

For M(ZAMS) > 27 $M_\odot$, all stars collapse into BHs. For metal-poor stars, the mass ranges of BHs are M(ZAMS) = 21–30 $M_\odot$, 40–50 $M_\odot$ and above 60 $M_\odot$. For most models above 30 $M_\odot$, $\xi_{2.5}$ of metal-poor stars shows a noticeable difference from solar-metallicity stars because the undershooting of H-rich envelope mixes some H into the He core and reduces the size of the He core. We will address the comparison of the evolution and core structure between two groups of models in a forthcoming paper.

6. BH Mass Distribution Spectrum

The mass range of BHs is limited by two mass gaps. The maximum mass of BHs, $M(\mathrm{BH})_{\max}$, is constrained by the lower edge of the PISN mass gap. In Section 4.1, $M(\mathrm{BH})_{\max} = 46\,M_\odot$ is suggested. The existence of another mass gap is claimed between the heaviest neutron stars (~2 $M_\odot$) and the lightest BHs (~5 $M_\odot$) (Özel et al. 2010; Farr et al. 2011) based on the dynamic mass measurements of about a dozen X-ray bursts.

Therefore, a BH mass distribution spectrum can be described based on M(ZAMS) as follows:

1. CCSN ($8 < M(\mathrm{ZAMS}) < 80\ M_\odot$): After Fe cores are formed, some progenitors explode and leave neutron stars (usually <25 $M_\odot$), while others collapse into BHs.
2. PPISN ($80 < M(\mathrm{ZAMS}) < 140\ M_\odot$): After several pulses during explosive oxygen burning, Fe cores are formed and collapse into smaller BHs due to mass ejection.
3. PISN ($140 < M(\mathrm{ZAMS}) < 300\ M_\odot$): Whole stars are disrupted by the thermonuclear explosions and no BHs left.

Figure 5 (left) shows the mass of BHs, M(BH), produced by all three groups of models 1–3 as a function of the initial He star mass M(He). For the CC case, M(He) is taken from the He core mass at the exhaustion of H. Due to the uncertainty in the BH formation process, M(BH) cannot be provided precisely. In the close binary systems, we assume that the H-rich envelope is stripped via mass loss by the stellar wind and Roche-lobe overflow. The upper and lower limits of M(BH) of each model are given by M(He) and M(CO), respectively, at the final stage, where M(CO) is the mass of the CO core, and we assume that at most the He layer could possibly be ejected during the BH formation.

Because stars with M(ZAMS) < 20 $M_\odot$ have $\xi_{2.5} < 0.278$, we assume that all stars with M(ZAMS) < 20 $M_\odot$ explode as supernovae and leave neutron stars. The smallest star that can collapse to a BH is ~20 $M_\odot$ with M(He) = 6.5 $M_\odot$ and M(CO) = 4.2 $M_\odot$ at the final stage. Thus, the lower limit of M(BH) is suggested to be 4.2 $M_\odot$. The largest star that collapses to a BH with CC is ~80 $M_\odot$ with M(He) = 38 $M_\odot$ and M(CO) = 33 $M_\odot$ at the final stage. Thus, the CCSN can produce BHs with a mass range of 4.2–38 $M_\odot$, while the stars that undergo PPISN may produce BHs with a mass range of 24–46 $M_\odot$ in this work. In Farmer et al. (2020) and Woosley & Heger (2021), BHs contributed by PPISN range 15–45 $M_\odot$ and 32–43 $M_\odot$, respectively.

According to our results, BHs with a mass range of 4.2–24 $M_\odot$ may be more likely to form only by CCSN, while BHs larger than 38 $M_\odot$ may be more likely to be produced by PPISN. BHs in the intermediate mass range (~24–38 $M_\odot$) may be contributed by both CCSN and PPISN. Most of the BBHs detected by LIGO are located in the mass range of 4.2–46 $M_\odot$.

One of the BH from GW170729 is likely to exceed this mass range, but we need to take into account the uncertainties in physics of stellar evolution models. Although BHs with M(BH) = 24–38 $M_\odot$ are contributed by both CCSN and PPISN, we may not ensure that BHs in this mass range have a larger birth possibility. According to the initial mass function,

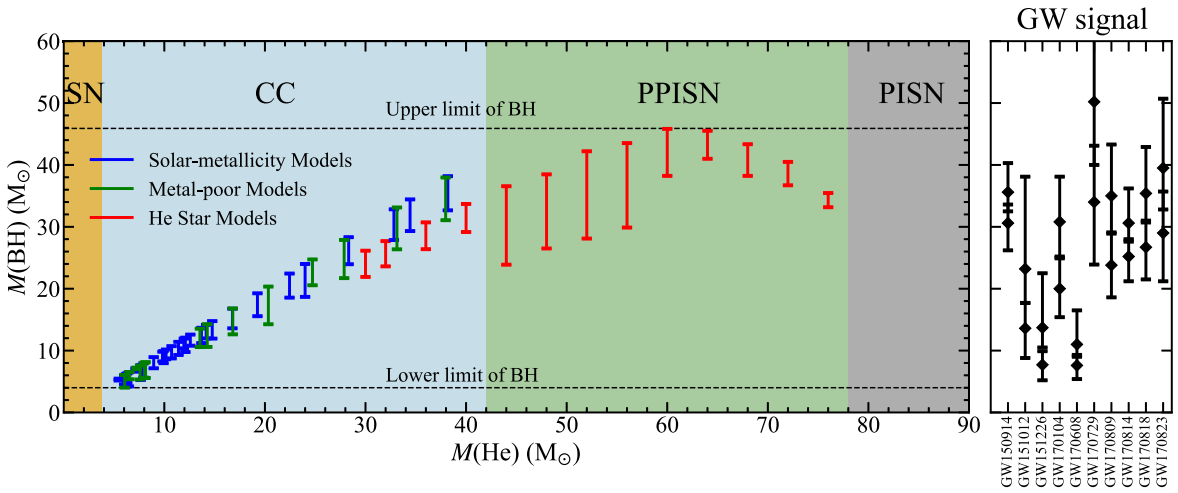

Figure 5. The BH masses M(BH) as a function of initial M(He). The solar-metallicity models, metal-poor models ($Z = 10^{-5}$) and He star models are shown with blue, green and red error bars, respectively. The upper limit and lower limit of the BH mass of each model are shown as the He core mass M(He) and CO core mass M(CO), respectively. The color regions show the M(He) range of the final fate: Fe CC, PPISN and PISN, respectively. The right panel shows the masses of BBHs detected by GWs from Abbott et al. (2019).

stars with higher mass may have a lower birth possibility. If we consider binary merging, the results would be more complex.

7. Conclusions

We calculated the evolution of He stars with the initial mass range of 30–120 $M_{\odot}$, which are produced in close binary systems. We studied particularly in detail the relation between convective carbon shell burning and the final fates of these He stars as follows:

1. Before the ignition of core oxygen burning, if $X(^{12}\mathrm{C})$ in the core is large enough, a convection zone forms above the carbon burning shell and extends to outer layers to mix carbon fuel to the carbon burning shell. Carbon shell burning becomes energetic and can heat the surrounding layers and retard the contraction of the oxygen core. Then, the star undergoes steady oxygen burning and CC.
2. If no convective carbon burning shell forms, the star undergoes explosive oxygen burning and PPIs.
3. During explosive oxygen burning, if the carbon burning shell can produce a convective region with a large-enough region, the energy produced by the core is efficiently transported by convection. Then, stars undergo PPISNe.
4. If no such convective shell appears, the accumulated energy in the core during explosive oxygen burning can disrupt the whole star as a PISN. For CCSNe in case 1 and PPISNe in cases 2 and 3, BHs are formed. We found that the mass range of BHs produced by PPISNe is 24–46 $M_{\odot}$.

For lower-mass stars with $M(\mathrm{ZAMS}) = 13$–$80\,M_{\odot}$, we calculated the evolution of H-rich stars from ZAMS to Fe CC. We distinguish these CCSN models by the compactness parameter $\xi_{2.5}$. By adopting the criterion that the models with $\xi_{2.5} > 0.278$ can collapse into BHs, we found that the mass range of BHs produced by these CCSNe is 4.2–38 $M_{\odot}$. Finally, by comparing the BH masses of the BBHs detected by LIGO, all of the observational results are consistent with the BH mass range predicted by our theoretical models.

Acknowledgments

This work was supported by the National Natural Science Foundation of China under Grant Nos. 11988101 and 11890694 and the National Key R&D Program of China No. 2019YFA0405502. K. Nomoto is supported by the World Premier International Research Center Initiative (WPI), MEXT, Japan, and the Japan Society for the Promotion of Science (JSPS) KAKENHI grants JP17K05382, JP20K04024 and JP21H04499.

References

Abbott, B. P., Abbott, R., Abbott, T. D., et al. 2016, PhRvL, 116, 061102
Abbott, B. P., Abbott, R., Abbott, T. D., et al. 2019, ApJL, 882, L24
Abbott, R., Abbott, T. D., Abraham, S., et al. 2020, ApJL, 900, L13
Anders, E., & Grevesse, N. 1989, GeCoA, 53, 197
Baraffe, I., Heger, A., & Woosley, S. E. 2001, ApJ, 550, 890
Barkat, Z., Rakavy, G., & Sack, N. 1967, PhRvL, 18, 379
Bond, J. R., Arnett, W. D., & Carr, B. J. 1984, ApJ, 280, 825
Buchmann, L., Azuma, R. E., Barnes, C. A., Humblet, J., & Langanke, K. 1996, PhRvC, 54, 393
Chen, K.-J., Woosley, S., Heger, A., Almgren, A., & Whalen, D. J. 2014, ApJ, 792, 28
Chieffi, A., Roberti, L., Limongi, M., et al. 2021, ApJ, 916, 79

Costa, G., Bressan, A., Mapelli, M., et al. 2021, MNRAS, 501, 4514
Cyburt, R. H., Amthor, A. M., Ferguson, R., et al. 2010, ApJS, 189, 240
de Jager, C., Nieuwenhuijzen, H., & van der Hucht, K. A. 1988, A&AS, 72, 259
Ertl, T., Janka, H. T., Woosley, S. E., Sukhbold, T., & Ugliano, M. 2016, ApJ, 818, 124
Farmer, R., Renzo, M., de Mink, S. E., Fishbach, M., & Justham, S. 2020, ApJL, 902, L36
Farmer, R., Renzo, M., de Mink, S. E., Marchant, P., & Justham, S. 2019, ApJ, 887, 53
Farr, W. M., Sravan, N., Cantrell, A., et al. 2011, ApJ, 741, 103
Fowler, W. A., & Hoyle, F. 1964, ApJS, 9, 201
Fuller, G. M., Fowler, W. A., & Newman, M. J. 1985, ApJ, 293, 1
Heger, A., & Woosley, S. E. 2002, ApJ, 567, 532
Kobulnicky, H. A., Kiminki, D. C., Lundquist, M. J., et al. 2014, ApJS, 213, 34
Kunz, R., Fey, M., Jaeger, M., et al. 2002, ApJ, 567, 643
Langanke, K., & Martínez-Pinedo, G. 2000, NuPhA, 673, 481
Leung, S.-C., Blinnikov, S., Ishidoshiro, K., Kozlov, A., & Nomoto, K. 2020, ApJ, 889, 75
Leung, S.-C., Nomoto, K., & Blinnikov, S. 2019, ApJ, 887, 72
Limongi, M., & Chieffi, A. 2015, in Chemical and Dynamical Evolution of the Milky Way and the Local Group, Proc. Sedem Conf., 15
Marchant, P., Renzo, M., Farmer, R., et al. 2019, ApJ, 882, 36
Moe, M., & Di Stefano, R. 2017, ApJS, 230, 15
Müller, B., Heger, A., Liptai, D., & Cameron, J. B. 2016, MNRAS, 460, 742
Nomoto, K., Kobayashi, C., et al. 2013, ARA&A, 51, 457
Nugis, T., & Lamers, H. J. G. L. M. 2000, A&A, 360, 227
O'Connor, E., & Ott, C. D. 2011, ApJ, 730, 70
Oda, T., Hino, M., Muto, K., Takahara, M., & Sato, K. 1994, ADNDT, 56, 231
Ohkubo, T., Nomoto, K., Umeda, H., Yoshida, N., & Tsuruta, S. 2009, ApJ, 706, 1184
Osaki, Y. 1966, PASJ, 18, 384
Özel, F., Psaltis, D., Narayan, R., & McClintock, J. E. 2010, ApJ, 725, 1918
Paxton, B., Bildsten, L., Dotter, A., et al. 2011, ApJS, 192, 3
Paxton, B., Cantiello, M., Arras, P., et al. 2013, ApJS, 208, 4
Paxton, B., Marchant, P., Schwab, J., et al. 2015, ApJS, 220, 15
Paxton, B., Schwab, J., Bauer, E. B., et al. 2018, ApJS, 234, 34
Paxton, B., Smolec, R., Schwab, J., et al. 2019, ApJS, 243, 10
Renzo, M., Ott, C. D., Shore, S. N., & de Mink, S. E. 2017, A&A, 603, A118
Sukhbold, T., & Adams, S. 2020, MNRAS, 492, 2578
Sukhbold, T., Ertl, T., Woosley, S. E., Brown, J. M., & Janka, H. T. 2016, ApJ, 821, 38
Sukhbold, T., Woosley, S. E., & Heger, A. 2018, ApJ, 860, 93
Toro, E. F., Spruce, M., & Speares, W. 1994, ShWav, 4, 25
Tumino, A., Spitaleri, C., La Cognata, M., et al. 2018, Natur, 557, 687
Tur, C., Heger, A., & Austin, S. M. 2007, ApJ, 671, 821
Umeda, H., & Nomoto, K. 2002a, ApJ, 565, 385
Umeda, H., & Nomoto, K. 2002b, ApJ, 565, 385
van Son, L. A. C., De Mink, S. E., Broekgaarden, F. S., et al. 2020, ApJ, 897, 100
Vink, J. S., de Koter, A., & Lamers, H. J. G. L. M. 2001, A&A, 369, 574
Wellstein, S., Langer, N., & Braun, H. 2001, A&A, 369, 939
Woosley, S. E. 2017, ApJ, 836, 244
Woosley, S. E., & Heger, A. 2007, PhR, 442, 269
Woosley, S. E., & Heger, A. 2021, ApJL, 912, L31